An Exact Method for Determining Local Solid Fractions in Discrete Element Method Simulations

Ben Freireich and Madhusudhan Kodam
School of Mechanical Engineering, Purdue University, West Lafayette, IN 47907

Carl Wassgren
School of Mechanical Engineering, Purdue University, West Lafayette, IN 47907

Dept. of Industrial and Physical Pharmacy, Purdue University, West Lafayette, IN 47907

DOI 10.1002/aic.12223
Published online April 20, 2010 in Wiley Online Library (wileyonlinelibrary.com).

A novel solid fraction algorithm is presented which accounts for the partial volume of a sphere straddling cuboidal bin boundaries. The algorithm accounts for spheres intersecting a single plane (face), two perpendicular planes (edge), or three perpendicular planes (corner). Comparisons are made against the more common algorithm in which the solid fraction is determined by assigning the sphere's total volume to the bin in which the sphere's center of volume (COV) is located. Bin size-to-sphere diameter ratios >30 must be used to give errors <5% when using the traditional method when applied to simple cubic (SC) and hexagonal packing assemblies. Bin size-to-sphere diameter ratios larger than five are required for random sphere packings. Although time averaged solid fraction measurements are similar using either the exact or COV solid fraction schemes, the scatter in the COV method is much larger than for the exact method. © 2010 American Institute of Chemical Engineers *AIChE J,* 56: 3036–3048, 2010

Keywords: solid fraction, packing fraction, volume fraction, porosity, discrete element method, DEM, simulation

Introduction

The solid fraction of a particulate assembly is a commonly measured quantity. The solid fraction, v, is defined as the ratio of the volume of a region occupied by particles, $V_{\text{particles}}$, to the total volume of the region, V_{region}:

$$v \equiv \frac{V_{\text{particles}}}{V_{\text{region}}}. \tag{1}$$

The solid fraction is arguably one of the most important parameters governing the statics and dynamics of particulate systems and, thus, an accurate measurement of this quantity is essential.

Correspondence concerning this article should be addressed to C. Wassgren at wassgren@purdue.edu.

A relatively recent, and increasingly more common tool used for studying particulate systems is discrete element method (DEM) computer simulation. In DEM, the forces acting on individual particles are determined using appropriate force models, particle accelerations are calculated using Newton's laws, and the resulting equations of motion are integrated in time to determine new particle states. The process is repeated until an ending condition, such as a maximum time, is reached. Because of the computational cost of contact detection, most DEM simulations model particles as spheres.

Solid fraction measurements in DEM simulations are straightforward to make, in principle. As all particle positions are known at each instant in time, the solid fraction in a specified volume can be calculated. Various techniques have been proposed for measuring solid fraction fields in DEM simulations. These techniques can be classified either as binning or smoothing methods.

Smoothing methods have been derived in an attempt to form Eulerian fields of macroscopic quantities, like bulk density, from the Lagrangian trajectories of individual particles. These techniques rely on spatial and temporal weighting and will not be specifically addressed in this work.[1–3]

In binning methods, the simulation domain is decomposed into smaller bins and the solid fraction is calculated by determining the volume each particle contributes to a bin. Several common algorithms have been proposed in the literature for this volume calculation depending upon the bin geometry and how an individual particle's volume contribution is calculated. These methods include: exact partial volume calculation using spherical, cylindrical, or circular bins, exact partial volume calculation using parallel strip bins, and approximate volume calculation using cuboidal bins.

A number of researchers, as well as a popular commercial DEM software package, determine solid fraction fields by calculating the exact partial volume that a spherical particle contributes to a spherical or cylindrical bin.[4–6] In this method, the particle volume can be divided into two subvolumes: the volume inside the bin and the volume outside it. For a spherical bin, the volume within the bin is given by:

$$V_{\text{included}} = \frac{\pi}{3} h_1^2 (3R - h_1) + \frac{\pi}{3} h_2^2 (3r - h_2) \tag{2}$$

where

$$h_1 = R - \frac{R^2 - r^2 + d^2}{2d} \quad \text{and} \tag{3}$$

$$h_2 = \frac{R^2 - r^2 + d^2}{2d} - (d - r). \tag{4}$$

The parameter R is the radius of the spherical bin, r is the radius of the particle, and d is the distance between the center of the bin and the particle. The formulas for a cylindrical bin are given in Mueller.[7] Although the calculation is straightforward, the method has an important drawback. To calculate a solid fraction field, contact detection between the spherical bin and all of the particles in the domain must be performed. These calculations can result in significant computational cost, especially if the calculations must be performed within the DEM simulation rather than during post processing.

A special case of the previously described algorithm occurs when the bins are annular or spherical rings, or strips, centered about some common point. When using such strips, the resulting solid fraction field is one-dimensional with variation along a radial coordinate. This approach has been used extensively in studies involving annular shear cells[8,9] and cylindrical beds.[7,10–13]

In their studies of two-dimensional annular shear cells, Lätzel et al.[14] used an approximate method for computing solid fraction. They approximated annular strips as rectangular ones and used the formula for a circular cap to find the particle partial areas. They also attempted to further simplify the calculation by neglecting the effects of the partial area altogether and simply included the entire particle's area in a bin if its center of area was in the bin. Comparing the partial area and center of area approaches, they concluded that for an annular bin width greater than the particle diameter, both methods return the same results when time averaged, although the center of area method results in far more scatter.

The rectangular strip approach is also used in many geometries naturally suited for one-dimensional solid fraction profiles. For example, in Couette flow or inclined plane simulations, the solid fraction variation perpendicular to a plane is of interest and rectangular strips are a natural choice for the bin geometry. Here, as with Lätzel et al.,[14] the partial volume contribution due to spheres intersecting the face of a bin are computed using a simple relation for the volume (or area) of a spherical (or circular) cap.[15–20] Some authors, most likely in an effort to save computational cost, use a center of volume (COV) approach.[21,22] Most authors fail to report their method of computing solid fraction profiles entirely.[23–35]

Louge[36] compared the COV and partial volume methods for parallel strips when determining the solid fraction profile in the vicinity of a boundary in a Couette flow. He argued that the COV method more closely matches the implied meaning of the distribution function in kinetic theory of granular flow formulations.[37] In particular, within one radius of a boundary, the COV method will always report that the local solid fraction is zero while a partial volume method smoothly increases from zero at the boundary. When time averaged, both methods give similar solid fractions far from the wall.

The use of cuboidal (or rectangular) bins for calculating three-dimensional (or two-dimensional) solid fraction fields has also been considered. For these bins, the computational complexity of accounting for partial particle volumes (or areas) increases considerably. In addition, the distribution of these partial volumes (or areas) into the neighboring bins must also be accounted for. This increase in computational complexity makes the COV (or area) approach much more attractive. Indeed, many authors and at least one commercial DEM software package report explicitly that they calculate solid fraction fields using such an approach.[38–41]

Hoomans et al.,[42] however, accounted for partial areas using a square grid with circular particles in their two-dimensional simulations of a fluidized bed. Their method exactly assigns partial areas to neighboring bins at bin faces and corners. The method was also approximately extended to three dimensions in quasi 2D simulations, but still used a two-dimensional grid of rectangular bins.[43] In the 3D implementation, the exact spherical cap volume is calculated when a particle intersects the face of a cubical bin. The partial sphere volume fraction due to intersection with two sides of a bin (i.e., an edge) is approximated as the product of the fractional volumes of the spherical caps overlapping each of the two bin sides. Intersection with three faces (i.e., a corner) is not considered.

Descriptions of the algorithms and formulas used for calculating the exact partial volumes of particles in spherical, cylindrical, annular, and rectangular strip bins have been presented in the literature. In addition, the approximate COV approach to calculating solid fractions has also been explicitly presented. However, an algorithm for calculating the exact partial volume using cuboidal bins has not been described in the literature. Such an algorithm is not trivial as it involves the calculation of partial volumes for face, edge,

and corner overlaps. Moreover, the distribution of partial volumes must be handled for 26 neighboring bins. This article presents just such an algorithm and compares the solid fraction fields using this exact method against the commonly used COV approach for regular, random, and time varying sphere packing arrangements.

Algorithm

In the following analysis, spherical particles, cuboidal measurement bins, and a Cartesian coordinate system are assumed. In addition, the smallest dimension of the bin is assumed to be larger than the diameter of the sphere. The implication of this last assumption is that a sphere can be in contact with at most three mutually perpendicular bin walls or planes (or sides). The total number of potential sphere/bin boundary overlap scenarios is four. This total includes cases involving no overlap with the bin boundaries, and overlap with bin sides (planes), edges, and corners.

Determining the type of overlap scenario

The first step in assigning the appropriate sphere volume to a particular bin is determining the type of sphere/bin overlap that occurs. The sphere's COV position is given by $\mathbf{x}_{\text{sphere}}$ and its radius is r. The corner of the bin with the smallest component positions is $\mathbf{x}_{\text{bin,min}}$ whereas the corner with the largest component positions is $\mathbf{x}_{\text{bin,max}}$. The vectors $\delta_{\min}$ and $\delta_{\max}$, defined as

$$\delta_{\min} = r\mathbf{1} - \left(\mathbf{x}_{\text{sphere}} - \mathbf{x}_{\text{bin,min}}\right), \tag{5}$$

$$\delta_{\max} = r\mathbf{1} - \left(\mathbf{x}_{\text{bin,max}} - \mathbf{x}_{\text{sphere}}\right), \tag{6}$$

where $\mathbf{1} = (1, 1, 1)$ is a vector, are used to determine if there is overlap with each of the bin sides. If a component of $\delta_{\min}$ or $\delta_{\max}$ has a positive value, then the sphere has an overlap with that particular bin face. A negative value implies no overlap.

Six Boolean variables, $x_{\min}$, $y_{\min}$, $z_{\min}$, $x_{\max}$, $y_{\max}$, and $z_{\max}$, are calculated for use in determining the number of bin planes in which the sphere is in contact. These variables are defined as:

$$\begin{aligned} x_{\min} &= \left(\hat{\mathbf{e}}_x \cdot \delta_{\min} > 0\right) \\ y_{\min} &= \left(\hat{\mathbf{e}}_y \cdot \delta_{\min} > 0\right) \\ &\vdots \\ z_{\max} &= \left(\hat{\mathbf{e}}_z \cdot \delta_{\max} > 0\right) \end{aligned} \tag{7}$$

where $\hat{\mathbf{e}}_x$, $\hat{\mathbf{e}}_y$, and $\hat{\mathbf{e}}_z$ are unit vectors in each of the coordinate directions. Given that a true Boolean variable value has a value of 1 whereas a false value is equal to 0, the number of sphere/bin face overlaps, $n\delta$, is:

$$n_\delta = x_{\min} + y_{\min} + z_{\min} + x_{\max} + y_{\max} + z_{\max}\,. \tag{8}$$

where $n_\delta \leq 3$. Note that these face overlap scenarios may also include edge and corner overlaps. The following sections describe how the sphere volume is partitioned for the various contact cases.

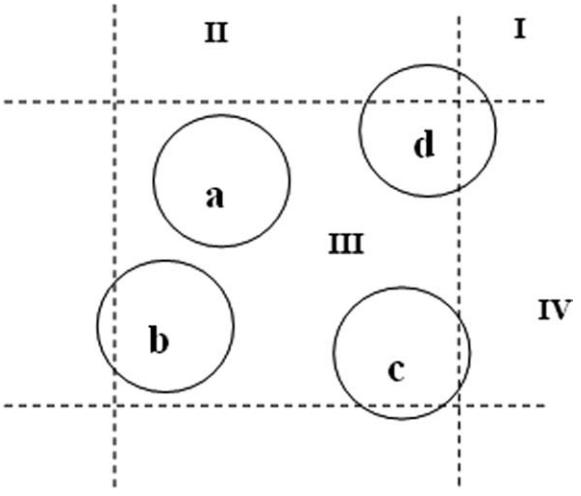

Figure 1. Different types of sphere overlaps with bin boundaries.

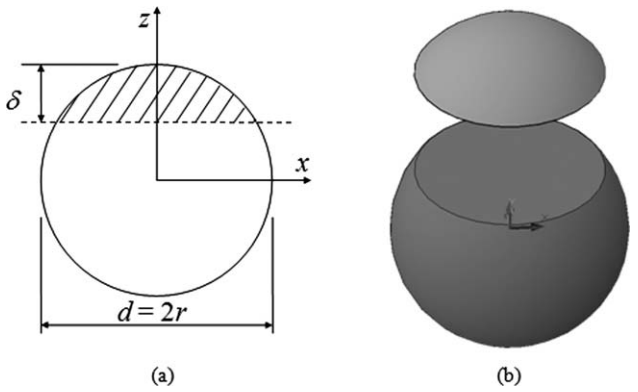

Figure 2. Schematic of a sphere overlapping with a single bin face.

(a) Two-dimensional view with dimensions and (b) three-dimensional view. The sphere diameter and radius are d and r, respectively, δ is the degree of overlap with the face (which is indicated by the dashed line), and z is the local coordinate direction normal to the face. The shaded region in (a) is the spherical cap volume calculated in Eq. 9.

No sphere/bin face overlaps ($n_\delta = 0$)

For this case (sphere a in Figure 1), the total sphere volume is simply added to the bin in which the bin COV is located.

Overlap with a single face ($n_\delta = 1$)

In the case of a single sphere/bin face overlap, the volume of the spherical cap that penetrates into a neighboring bin must be calculated (sphere b in Figure 1). The spherical cap volume may be determined in terms of the overlap magnitude and sphere radius using calculus:

$$V_{\text{face}} = \int_{r-\delta}^{r}\int_{0}^{2\pi}\int_{0}^{\sqrt{r^2-z^2}} \rho d\rho d\theta dz = \tfrac{\pi}{3}\delta^2(3r-\delta), \tag{9}$$

where ρ and θ are the radial and azimuthal cylindrical polar coordinate angles, z is the coordinate normal to the plane, and δ is the overlap between the sphere and the plane (Figure 2):

$$\delta = \delta_{\min\,/\,\max} \cdot \hat{\mathbf{e}}_i \tag{10}$$

where min or max and i are chosen according to the face that is overlapped.

It is more convenient for curve fitting purposes to normalize Eq. 9 using the sphere's total volume:

$$\frac{V_{\text{face}}}{\frac{4}{3}\pi r^3} = f_{\text{face}}\left(\frac{\delta}{r}\right), \tag{11}$$

where

$$f_{\text{face}}\left(\frac{\delta}{r}\right) = \frac{1}{4}\left[3\left(\frac{\delta}{r}\right)^2 - \left(\frac{\delta}{r}\right)^3\right], \tag{12}$$

and δ/r is the relative overlap between the sphere and plane. The fractional sphere volume in the bin in which the sphere's center is located, V_{bin}, is simply the sphere's total volume minus the cap volume. Expressed in dimensionless form:

$$\frac{V_{\text{bin}}}{\frac{4}{3}\pi r^3} = 1 - f_{\text{face}}\left(\frac{\delta}{r}\right). \tag{13}$$

Overlap with two faces ($n_\delta = 2$)

Two subcases must be considered for the case of two face overlaps. The first possibility is that the common edge between the two faces does not intersect the sphere (sphere c in Figure 1). For this case, the sphere volume is distributed among three bins: the bin in which the sphere center is located, and the neighboring bins containing the spherical caps.

The second case occurs when the common edge intersects the sphere (sphere d in Figure 1) and the sphere volume must be distributed among four bins. As in the previous section, the volume contained in the edge region (Region I for sphere d in Figure 1) may be found using calculus; however, the calculations are tedious and, thus, are given in Appendix A rather than being presented here. For convenience, the final relation is given here:

$$\frac{V_{\text{edge}}}{\frac{4}{3}\pi r^3} = f_{\text{edge}}\left(\frac{\delta_1}{r}, \frac{\delta_2}{r}\right) \tag{14}$$

where δ_1 and δ_2 are the overlaps with the two bin faces (Figure 3). The function, f_{edge} is given by:

$$f_{\text{edge}}\left(\frac{\delta_1}{r}, \frac{\delta_2}{r}\right) = \begin{cases} \frac{1}{4\pi}\left[2\hat{a}\hat{b}\hat{x} - (3\hat{a} - \hat{a}^3)\tan^{-1}\left(\frac{\hat{x}}{\hat{b}}\right) - (3\hat{b} - \hat{b}^3)\tan^{-1}\left(\frac{\hat{x}}{\hat{a}}\right) + 2\tan^{-1}\left(\hat{x}\frac{\hat{a}}{\hat{b}}\right) + 2\tan^{-1}\left(\hat{x}\frac{\hat{b}}{\hat{a}}\right)\right] & \text{for } \hat{x}^2 > 0 \\ 0 & \text{for } \hat{x}^2 \le 0 \end{cases}. \tag{15}$$

where

$$\hat{a} \equiv 1 - \frac{\delta_1}{r}, \tag{16}$$

$$\hat{b} \equiv 1 - \frac{\delta_2}{r}, \quad \text{and} \tag{17}$$

$$\hat{x}^2 = 1 - \hat{a}^2 - \hat{b}^2. \tag{18}$$

Note that $\hat{x}^2 > 0$ corresponds to the case where the edge intersects the sphere whereas $\hat{x}^2 \le 0$ is the case when the sphere contacts the two faces, but not the edge. Note that $f_{\text{edge}} = [1/2]f_{\text{face}}$ when either δ_1 or δ_2 equal r.

The fractional sphere volume within the bin containing the sphere's COV is:

$$\frac{V_{\text{bin}}}{\frac{4}{3}\pi r^3} = 1 - \left[f_{\text{face}}\left(\frac{\delta_1}{r}\right) + f_{\text{face}}\left(\frac{\delta_2}{r}\right) - f_{\text{edge}}\left(\frac{\delta_1}{r}, \frac{\delta_2}{r}\right)\right]. \tag{19}$$

The dimensionless volumes in the neighboring bins corresponding to the δ_1 and δ_2 overlaps (Quadrants II and IV for sphere d in Figure 1) are:

$$\frac{V_{\delta_1}}{\frac{4}{3}\pi r^3} = f_{\text{face}}\left(\frac{\delta_1}{r}\right) - f_{\text{edge}}\left(\frac{\delta_1}{r}, \frac{\delta_2}{r}\right) \tag{20}$$

and,

$$\frac{V_{\delta_2}}{\frac{4}{3}\pi r^3} = f_{\text{face}}\left(\frac{\delta_2}{r}\right) - f_{\text{edge}}\left(\frac{\delta_1}{r}, \frac{\delta_2}{r}\right). \tag{21}$$

Overlap with a corner ($n_\delta = 3$)

The parameters for calculating the fractional sphere volume for a corner overlap are shown in Figure 4. The partial sphere volume located in the corner region (hatched region in Figure 4) is derived in Appendix A and is given by:

$$\frac{V_{\text{corner}}}{\frac{4}{3}\pi r^3} = f_{\text{corner}}\left(\frac{\delta_1}{r}, \frac{\delta_2}{r}, \frac{\delta_3}{r}\right) \tag{22}$$

where δ_1, δ_2, and δ_3 are the sphere overlaps with each of the three bin faces, and

$$f_{\text{corner}}\left(\frac{\delta_1}{r}, \frac{\delta_2}{r}, \frac{\delta_3}{r}\right) = \begin{cases} \frac{1}{2}f_{\text{edge}}\left(\frac{\delta_1}{r}, \frac{\delta_2}{r}\right) - \frac{1}{8\pi}\left\{\begin{array}{l} 6\hat{a}\hat{b}\hat{c} - 2\hat{a}\hat{A}\hat{c} - 2\hat{b}\hat{B}\hat{c} - (3\hat{b} - \hat{b}^3)\tan^{-1}\left(\frac{\hat{c}}{\hat{B}}\right) - (3\hat{a} - \hat{a}^3)\tan^{-1}\left(\frac{\hat{c}}{\hat{A}}\right) \\ +(3\hat{c} - \hat{c}^3)\left[\tan^{-1}\left(\frac{\hat{A}}{\hat{a}}\right) - \tan^{-1}\left(\frac{\hat{b}}{\hat{B}}\right)\right] + 2\left[\tan^{-1}\left(\hat{c}\frac{\hat{a}}{\hat{A}}\right) + \tan^{-1}\left(\hat{c}\frac{\hat{b}}{\hat{B}}\right)\right] \end{array}\right\} & \text{for } \hat{a}^2 + \hat{b}^2 + \hat{c}^2 < 1 \\ 0 & \text{for } \hat{a}^2 + \hat{b}^2 + \hat{c}^2 \ge 1 \end{cases} \tag{23}$$

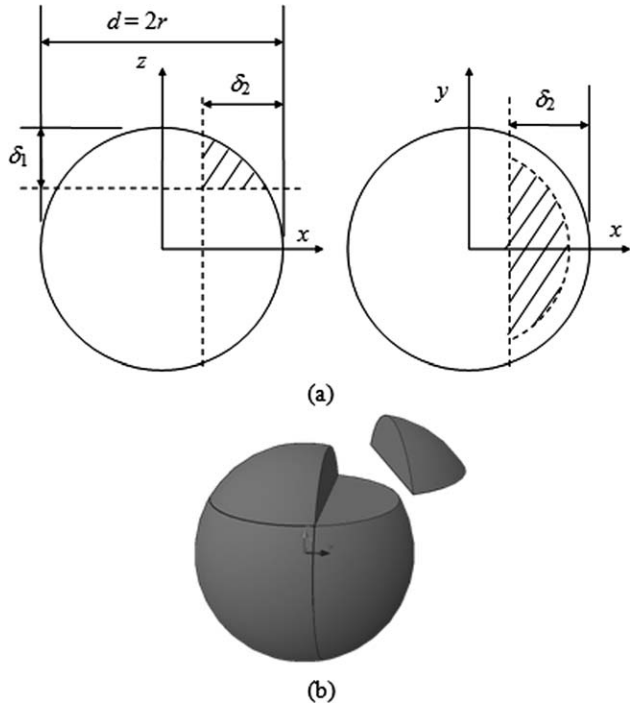

Figure 3. Schematic of a sphere overlapping with two faces and an edge.

(a) Two-dimensional view with dimensions and (b) three-dimensional view.

where the relations for $\hat{a}$ and $\hat{b}$ are stated in Eqs. 16 and 17, and

$$\hat{c} \equiv 1 - \frac{\delta_3}{r}, \tag{24}$$

$$\hat{A} \equiv \sqrt{1 - \hat{a}^2 - \hat{c}^2}, \quad \text{and} \tag{25}$$

$$\hat{B} \equiv \sqrt{1 - \hat{b}^2 - \hat{c}^2}. \tag{26}$$

Note that the sphere does not overlap the corner when $\hat{a}^2 + \hat{b}^2 + \hat{c}^2 \geq 1$. Furthermore, when δ_1, δ_2, or δ_3 equal r, Eq. 23 simplifies to $[1/2]f_{\text{edge}}$ with the remaining two overlaps as the arguments.

The fractional sphere volume contributing to the bin containing the sphere's center is,

$$\frac{V_{\text{bin}}}{\frac{4}{3}\pi r^3} = 1 - \left[f_{\text{face}}\left(\frac{\delta_1}{r}\right) + f_{\text{face}}\left(\frac{\delta_2}{r}\right) + f_{\text{face}}\left(\frac{\delta_3}{r}\right) - f_{\text{edge}}\left(\frac{\delta_1}{r}, \frac{\delta_2}{r}\right) - f_{\text{edge}}\left(\frac{\delta_1}{r}, \frac{\delta_3}{r}\right) - f_{\text{edge}}\left(\frac{\delta_2}{r}, \frac{\delta_3}{r}\right) + f_{\text{corner}}\left(\frac{\delta_1}{r}, \frac{\delta_2}{r}, \frac{\delta_3}{r}\right) \right]. \tag{27}$$

There are six additional partial volumes that must be calculated (Eqs. 22 and 27 account for the corner and COV regions, respectively). Three of the remaining regions overlap a face whereas the last three overlap an edge. The partial volume in the neighboring bin for which the face overlap has a magnitude of δ_1 is:

$$\frac{V_{\delta_1}}{\frac{4}{3}\pi r^3} = f_{\text{face}}\left(\frac{\delta_1}{r}\right) - f_{\text{edge}}\left(\frac{\delta_1}{r}, \frac{\delta_2}{r}\right) - f_{\text{edge}}\left(\frac{\delta_1}{r}, \frac{\delta_3}{r}\right) + f_{\text{corner}}\left(\frac{\delta_1}{r}, \frac{\delta_2}{r}, \frac{\delta_3}{r}\right). \tag{28}$$

Similarly, the partial volumes for the neighboring bins with face overlaps of δ_2 and δ_3 are:

$$\frac{V_{\delta_2}}{\frac{4}{3}\pi r^3} = f_{\text{face}}\left(\frac{\delta_2}{r}\right) - f_{\text{edge}}\left(\frac{\delta_1}{r}, \frac{\delta_2}{r}\right) - f_{\text{edge}}\left(\frac{\delta_2}{r}, \frac{\delta_3}{r}\right) + f_{\text{corner}}\left(\frac{\delta_1}{r}, \frac{\delta_2}{r}, \frac{\delta_3}{r}\right) \tag{29}$$

and,

$$\frac{V_{\delta_3}}{\frac{4}{3}\pi r^3} = f_{\text{face}}\left(\frac{\delta_3}{r}\right) - f_{\text{edge}}\left(\frac{\delta_1}{r}, \frac{\delta_3}{r}\right) - f_{\text{edge}}\left(\frac{\delta_2}{r}, \frac{\delta_3}{r}\right) + f_{\text{corner}}\left(\frac{\delta_1}{r}, \frac{\delta_2}{r}, \frac{\delta_3}{r}\right). \tag{30}$$

The partial volume that overlaps the edge common to the δ_1 and δ_2 faces is:

$$\frac{V_{\delta_1\delta_2}}{\frac{4}{3}\pi r^3} = f_{\text{edge}}\left(\frac{\delta_1}{r}, \frac{\delta_2}{r}\right) - f_{\text{corner}}\left(\frac{\delta_1}{r}, \frac{\delta_2}{r}, \frac{\delta_3}{r}\right). \tag{31}$$

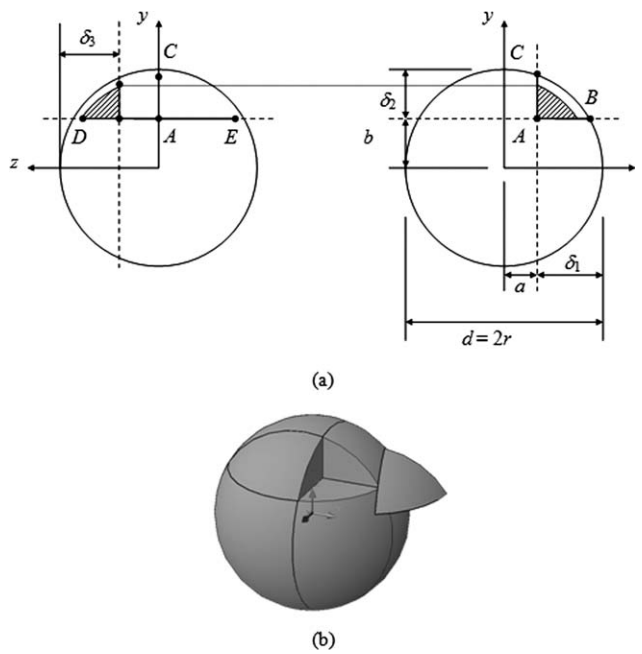

Figure 4. Schematic of a sphere overlapping with three faces and a corner.

(a) Two-dimensional view with dimensions and (b) three-dimensional view.

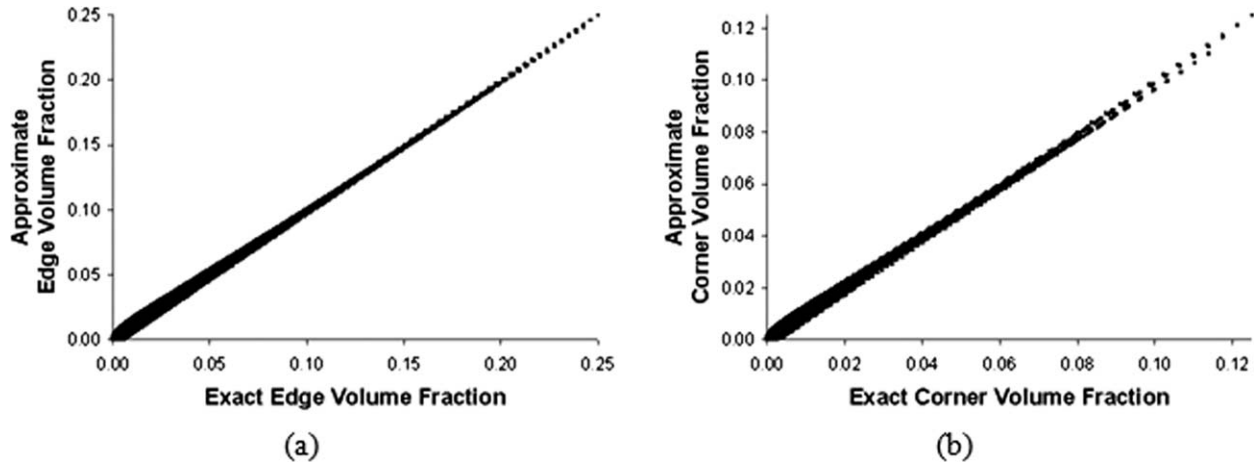

Figure 5. Curve fit volume fraction plotted against exact volume fraction for (a) edge and (b) corner cases.

Similarly,

$$\frac{V_{\delta_2\delta_3}}{\frac{4}{3}\pi r^3} = f_{\text{edge}}\left(\frac{\delta_2}{r},\frac{\delta_3}{r}\right) - f_{\text{corner}}\left(\frac{\delta_1}{r},\frac{\delta_2}{r},\frac{\delta_3}{r}\right) \tag{32}$$

and,

$$\frac{V_{\delta_1\delta_3}}{\frac{4\pi}{3}r^3} = f_{\text{edge}}\left(\frac{\delta_1}{r},\frac{\delta_3}{r}\right) - f_{\text{corner}}\left(\frac{\delta_1}{r},\frac{\delta_2}{r},\frac{\delta_3}{r}\right). \tag{33}$$

Curve fits to the volume calculations

Equation 15 involves several inverse tangent functions which are computationally time consuming. To avoid using these functions, a curve fit to the exact calculations has been developed. Note that the limiting behavior when either overlap vanishes, Eq. 15 reduces to half the face overlap volume (Eq. 11). A reasonable curve fit is then,

$$f_{\text{edge}}\left(\frac{\delta_1}{r},\frac{\delta_2}{r}\right) \approx a_1 f_{\text{face}}\left(\frac{\delta_1}{r}\right) + a_2 f_{\text{face}}\left(\frac{\delta_2}{r}\right) + a_{12} f_{\text{face}}\left(\frac{\delta_1}{r}\right) f_{\text{face}}\left(\frac{\delta_2}{r}\right). \tag{34}$$

A linear regression results in $a_1 = a_2 = -0.010987$ and $a_{12} = 1.0383$ with an R^2 value of 0.9959. A plot showing the curve fit plotted against the exact solution (Eqs. 15 and 34, respectively) is shown in Figure 5a. The average error in the fit relative to the exact function over the range $0 \le \delta_1/r < 1$ and $0 \le \delta_2/r < 1$ is 0.0007 with a maximum error of 0.007 at $(\delta_1/r, \delta_2/r) = (0.5, 0.5)$. The large relative error at smaller overlap values is not significant in an absolute sense since at small overlaps, the partial volume contained in the overlaps is relatively small. Implementing Eqs. 15 and 34 in a C++ program and using the clock function, Eq. 34 is found to be ~30% faster to calculate than Eq. 15.

A similar approach is used to fit the exact corner volume fraction f_{corner}:

$$f_{\text{corner}}\left(\frac{\delta_1}{r},\frac{\delta_2}{r},\frac{\delta_3}{r}\right) \approx a_1 f_{\text{face}}\left(\frac{\delta_1}{r}\right) + a_2 f_{\text{face}}\left(\frac{\delta_2}{r}\right) + a_3 f_{\text{face}}\left(\frac{\delta_3}{r}\right) + a_{12} f_{\text{face}}\left(\frac{\delta_1}{r}\right) f_{\text{face}}\left(\frac{\delta_2}{r}\right) + a_{13} f_{\text{face}}\left(\frac{\delta_1}{r}\right) f_{\text{face}}\left(\frac{\delta_3}{r}\right) + a_{23} f_{\text{face}}\left(\frac{\delta_2}{r}\right) f_{\text{face}}\left(\frac{\delta_3}{r}\right) + a_{123} f_{\text{face}}\left(\frac{\delta_1}{r}\right) f_{\text{face}}\left(\frac{\delta_2}{r}\right) f_{\text{face}}\left(\frac{\delta_3}{r}\right). \tag{35}$$

A least squares regression gives $a_1 = a_2 = a_3 = -0.001918$, $a_{12} = a_{13} = a_{23} = -0.006951$, and $a_{123} = 1.0355$, with an R^2 value of 0.9888. Figure 5b plots the exact value (Eq. 27) as a function of the curve fit (Eq. 35) over a range of overlaps. The average error is 0.0003 with the maximum error of 0.0036 occurring at small overlap values. Again, when implemented in C++, Eq. 35 is ~35% faster than Eq. 23.

Comparison of exact and COV solid fraction methods

The exact method for calculating the solid fraction described in the previous section is now compared to the more common COV method in which the total sphere volume is included in the bin containing the sphere's COV. Two well-defined static packing arrangements are considered first: simple cubic (SC) and hexagonal close packing (HCP) of identical spheres (Figures 6a, b). The solid fraction is measured in cubical bins for these packings as a function of the bin-to-sphere size ratio, a/d, where a is the bin side length and d is the sphere diameter. The origin of the measurement bin is such that the first sphere within the bin is always fully contained within the bin, i.e., the location of the center of the first sphere with respect to the origin of the measurement bin is $[\mathbf{1/2}]d(1, 1, 1)$ (refer to Figure 6). Offsetting the origin of the measurement bin slightly alters the solid fraction vs. (a/d) curve, but does not change the nature of the results. For reference, the exact solid fraction for a SC unit cell is $v_{\text{SC}} = 0.524$ whereas the HCP unit cell solid fraction is $v_{\text{HCP}} = 0.741$.

Figure 7a plots the solid fraction as a function of the relative bin size using the COV and exact methods for the SC

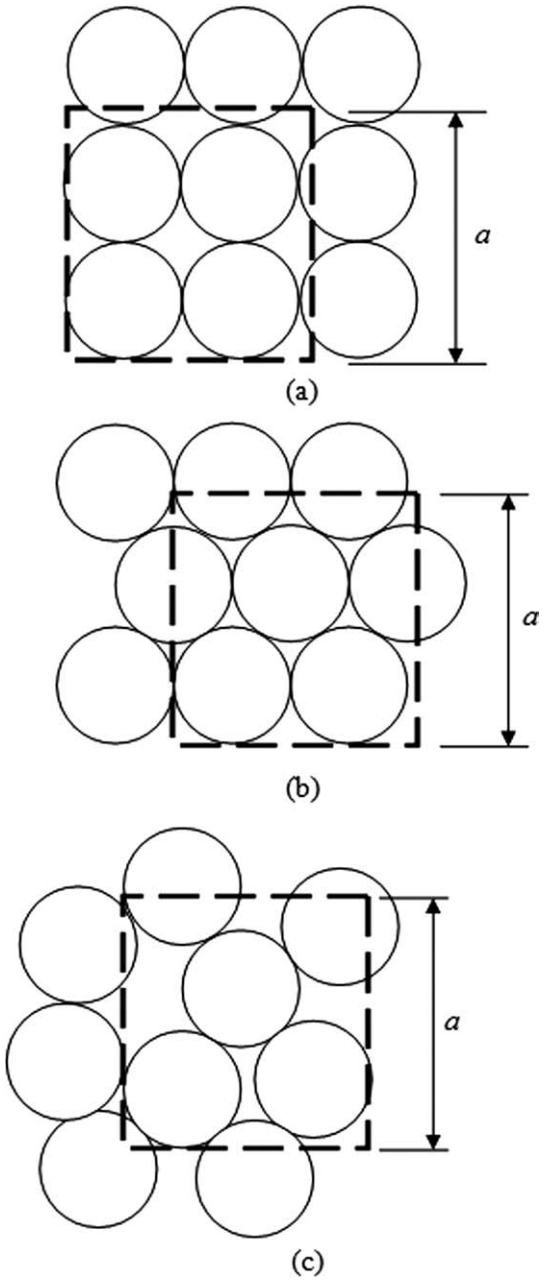

Figure 6. Two-dimensional schematics for (a) a SC packing, (b) a HCP, and (c) a random packing.

The figures also show an example of a measurement bin with side length a.

packing. The COV method shows significant deviations from the unit cell solid fraction value with non-physical values >1 for $1.5 < a/d < 1.62$. Discontinuous solid fraction values also appear as the measurement bin size becomes just large enough to include the center of new spheres and, thus, the solid fraction abruptly increases due to the addition of the total volume of the newly included spheres. As a/d increases, the COV method produces a solid fraction approaching the unit cell SC value as anticipated, but even when $a/d \approx 10$ the relative difference between the COV method and the exact method, $(\nu_{COV}-\nu_{Exact})/\nu_{Exact}$, can be as large as 20% (refer to Figure 8a).

The solid fraction using the exact algorithm fluctuates sinusoidally with a periodicity of one, as expected. When the measurement bin size corresponds exactly to the SC unit cell, both methods give the same solid fraction as the unit cell value. The exact algorithm converges to the unit cell value much more rapidly than the COV method (Figure 7a).

The solid fraction trends for the HCP packing (Figures 7b, 8b) are similar to those observed for the SC lattice. One significant difference, however, is that for the HCP lattice, the solid fraction appears to vary in a more irregular fashion than for the SC case. An expanded view of the solid fraction over a wider range of a/d for the exact method is shown in Figure 9. In addition to a wavelength corresponding to the sphere diameter, a beat frequency is also observed. This beat frequency is the result of a secondary intrinsic length scale in the HCP lattice. Unlike the SC lattice which has only a single length scale corresponding to the sphere diameter, the HCP lattice has several length scales due to how the spheres pack. The vertices corresponding to the HCP lattice cell are located at the following (dimensionless) coordinate locations relative to the measurement bin origin: (0, 0, 0), (1, 0, 0), (1/2, $3^{1/2}$/2, 0), and (1/2, $3^{1/2}$/6, $6^{1/2}$/3). Thus, the function giving the exact solid fraction as a function of the bin length will be comprised of sinusoids with wavelengths equaling these cell lengths. A Fourier transform of the solid fraction as a function of bin length is shown in Figure 10. Peaks in the signal appear at each of the reciprocals of the vertex components. The beating phenomenon observed in Figure 9 is the result of superimposing two periodic functions with nearly equal frequencies, with the beat frequency approximately equal to the differences in the two frequencies. Of the given cell lengths, the wavelengths corresponding to the $6^{1/2}$/3 and $3^{1/2}$/2 dimensions are the closest and, thus, an anticipated beat wavelength of:

$$\left[\left(\frac{\sqrt{6}}{3}\right)^{-1}-\left(\frac{\sqrt{3}}{2}\right)^{-1}\right]^{-1}\approx 14.3 \tag{36}$$

is expected, which indeed matches the beat period shown in Figure 9.

In addition to regular packing arrangements, the COV and exact solid fraction algorithms were compared for randomly generated packing arrangements of uniform spheres. The algorithm used here for creating cubical, periodic packings proceeds as follows.

(1) Calculate the linear dimension of the cube required to give the desired total solid fraction given the prescribed particle size and number of particles.

(2) Initialize all particle diameters to half their intended diameter, d_{final}.

(3) Randomly choose three Cartesian coordinates within the domain.

(4) Ensure that a particle placed at the chosen coordinates does not contact a previously placed particle or their periodic reflections. If a contact occurs, repeat the previous step, if not proceed to the following step.

(5) Place all particles in the domain according to the two previous steps.

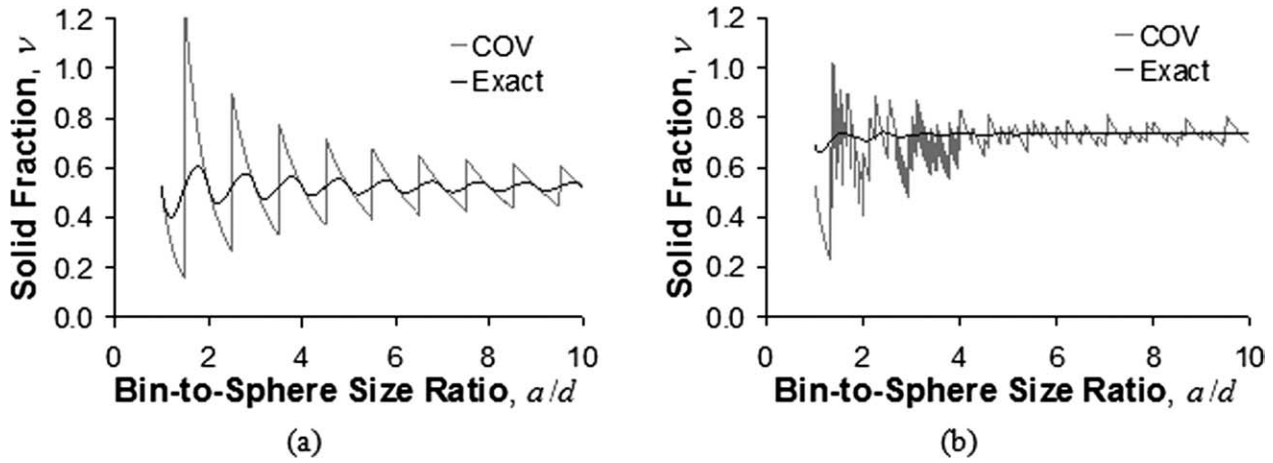

Figure 7. Solid fraction plotted as a function of bin-to-sphere size ratio using the exact and COV methods for an (a) SC lattice and (b) HCP lattice.

(6) Iterate in time, t, using a standard DEM algorithm, but with particle diameters increasing according to $d = d_{\text{final}}*[1-\exp(-t/\tau)]$ where τ is a constant.

(7) When $d > 0.99d_{\text{final}}$, set $d = d_{\text{final}}$ and output the particle states.

The solid fraction as a function of bin size for the one particular random packing with solid fraction of 0.55 is shown in Figure 11a. Here, the same trends are observed as in the two previous cases: large errors and fluctuations are observed using the COV method. One distinguishing feature of random packings is that the relative error in solid fraction decreases much more rapidly than in either the SC or HCP lattice cases. In all of the random packing studies performed using the previously described algorithm, both the exact and COV methods showed a relative difference of $\leq 5\%$ beyond a dimensionless bin size of $\sim a/d = 5$ (Figure 11b).

In addition to static arrangements, the COV and exact solid fraction methods were applied to dynamic systems. As a case study, the DEM simulation data for spheres tumbling in a rotating drum obtained from Freireich et al.[44] (Figure 12) was examined. A cubical measurement bin was located slightly below the free surface with $a/d = 1.5$, equal to the typical value used by Yang[26] who studied the same geometry. The instantaneous solid fraction was measured over several drum revolutions using both the exact and COV methods. The results are shown in Figure 13a. The COV method shows significantly more scatter than the exact method. Furthermore, the COV method results in a solid fraction greater than unity at several instances.

Figure 13a suggests that the time averaged values using either method are nearly equivalent. Figure 13b shows the time averaged solid fractions measurements for both methods for several dimensionless bin sizes. The scatter bars include 90% of all the solid fraction measurements over eight revolutions. For small bin sizes, the COV and exact methods agree on average, but show widely different instantaneous results. This effect is likely to be important in unsteady simulations such as dynamic clustering,[45] fluidized beds,[42] or dense phase pneumatic conveying.[46] The scatter decreases for both methods as the dimensionless bin size increases. For the bin sizes examined, the scatter using the exact method was approximately one-third of the scatter using the COV method.

The increase in accuracy achieved with the exact method comes at a higher computational cost. Specifically, the time

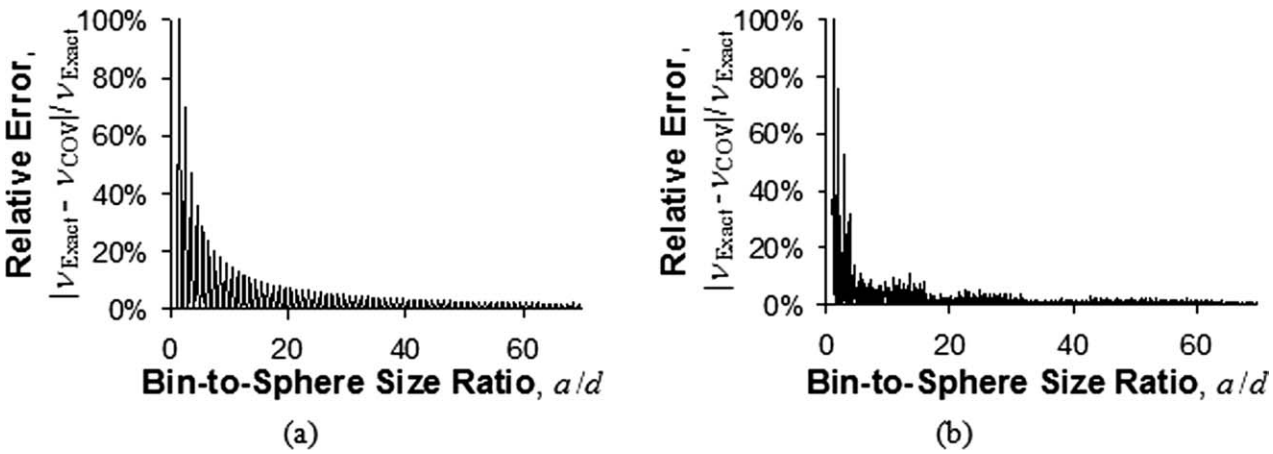

Figure 8. Relative error in COV method as a function of bin-to-sphere size ratio for an (a) SC lattice and (b) HCP lattice.

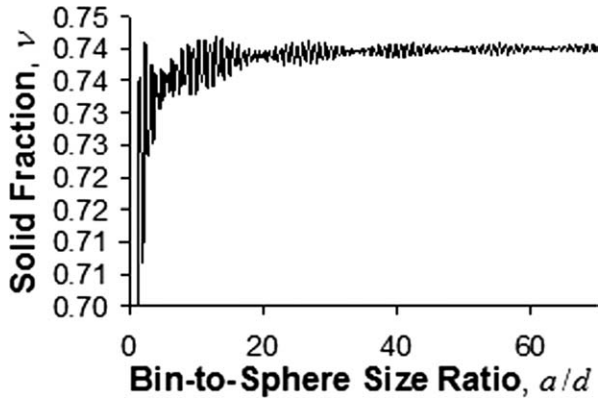

Figure 9. Solid fraction plotted as a function of the bin-to-sphere size ratio for an HCP lattice.

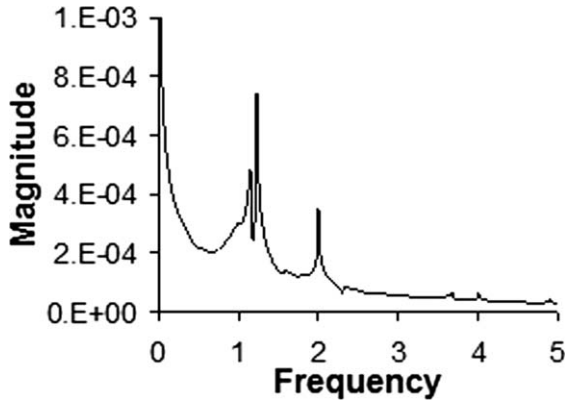

Figure 10. Fourier transform of the exact solid fraction as a function of bin-to-sphere size ratio given in Figure 7b.

to compute the solid fraction for the previous examples using the exact method required 230%, 130%, and 50% more time than using the COV method for $a/d = 1.0$, 1.5, and 2.0, respectively. As a/d grows, the difference in computational time between methods decreases because the number of spheres intersecting the surface of the region as compared to those residing in the bulk of the region decreases. For a typical bin size of $a/d = 1.5$, the exact method requires roughly twice as much time as the CoV method. However, this is only a comparison of the time to compute the solid fraction in a DEM simulation, and not the total DEM computational time. The other computations in a DEM simulation require significantly longer time than the solid fraction calculations, so that the total computational cost is negligibly affected.

The time increases reported in the previous paragraph are determined by comparing the time to compute the solid fraction when both methods use the same bin size. A fairer approach is to compare them for the same effective bin size. As has been shown, for any desired level of accuracy the COV method requires a larger bin size than the exact method. For example, Figure 13b shows that the accuracy (scatter) observed using the exact method at $a/d = 1.0$ is comparable to that observed using the COV method at an $a/d = 2.0$. In this case, using a bin size of $a/d = 1.0$ and the exact method is 50% faster per bin than using the comparable COV method with an $a/d = 2.0$. Therefore, using the exact method with a relatively smaller bin size has dual advantages; it increases computational efficiency and also the spatial resolution.

Obviously, a smaller bin size will result in a higher spatial resolution. For non-overlapping bins, smaller bins improve spatial resolution by allowing more measurements in a given volume. Gradients in solid fraction cannot be observed on scales equal to or smaller than the bin size. For a given accuracy, the COV method will always have a smaller spatial resolution than the exact method because the COV method requires a larger bin size. The number of measurements in a given volume may be increased at a fixed bin size by allowing bins to overlap. However, even allowing overlaps, large bins are unable to resolve variations in solid fraction. This effect becomes clearer when the bin is thought of as an averaging volume. Also, overlapping bins inherently give lower resolution near boundaries.

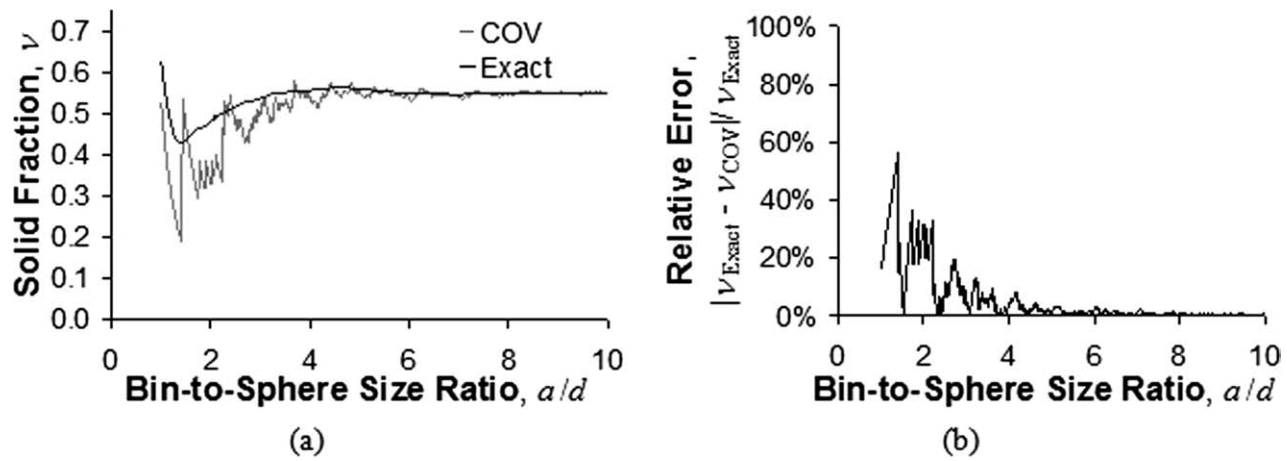

Figure 11. (a) Solid fraction and (b) relative error as a function of bin-to-sphere size ratio using the exact and COV methods for a random packing with an overall solid fraction of $\nu = 0.55$.

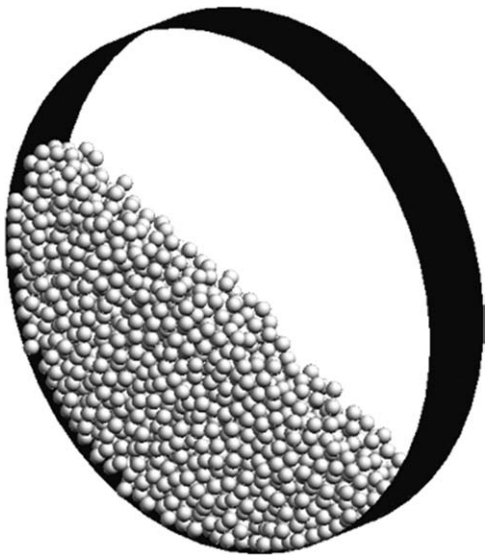

Figure 12. A snapshot from the rotating drum simulation of Freireich et al.[44]

Conclusions

An exact method for calculating the solid fraction of spheres located within cuboidal measurement bins has been presented. In addition to the exact formulas for calculating partial volumes, curve fits to the formulas are also presented. The curve fits are accurate approximations to the exact formulas (the curve fits have R^2 values >0.98), yet are $\sim$30–35% faster to calculate.

Comparisons between the exact method and the more traditional, COV solid fraction method show that large errors occur when applying the COV method to static assemblies of spheres using small measurement bin size-to-sphere diameter ratios. For SC and HCP lattices, bin-to-sphere size ratios greater than $\sim$30 must be used to keep the error in the COV method $\leq$5%. For random packings using the algorithm described in the text, bin-to-sphere size ratios greater than roughly five must be used to give an error $\leq$5% using the COV method.

The time averaged solid fraction of a dynamic particle assembly was nearly equal using either the exact or COV methods. However, the error in the instantaneous solid fractions using the COV method resulted in the scatter of the solid fraction being approximately three times larger than when the exact method is used.

For a fixed bin size, the exact method requires more computational time than the COV method. However, for a desired level of accuracy, the exact method is computationally more efficient per bin due to the smaller bin size required. Furthermore, the time to compute the solid fraction using either method is negligibly small compared to the rest of the DEM calculations.

Although the COV method is simpler to implement than the exact method, the large bin sizes required to minimize the error in the solid fraction calculation make the method less useful since the spatial resolution using the method is significantly degraded. Although the time-averaged solid fraction using the COV matches the exact method well, the scatter in the solid fraction measurements is large due to the error in the COV method. The exact method, and in particular the curve, fits to the exact formulas, are still relatively simple to implement and avoid the significant errors produced by the COV method. Furthermore, using the exact method with a relatively smaller bin size has a several advantages: it increases computational efficiency per bin, gives more accurate instantaneous measurements, and improves the spatial resolution.

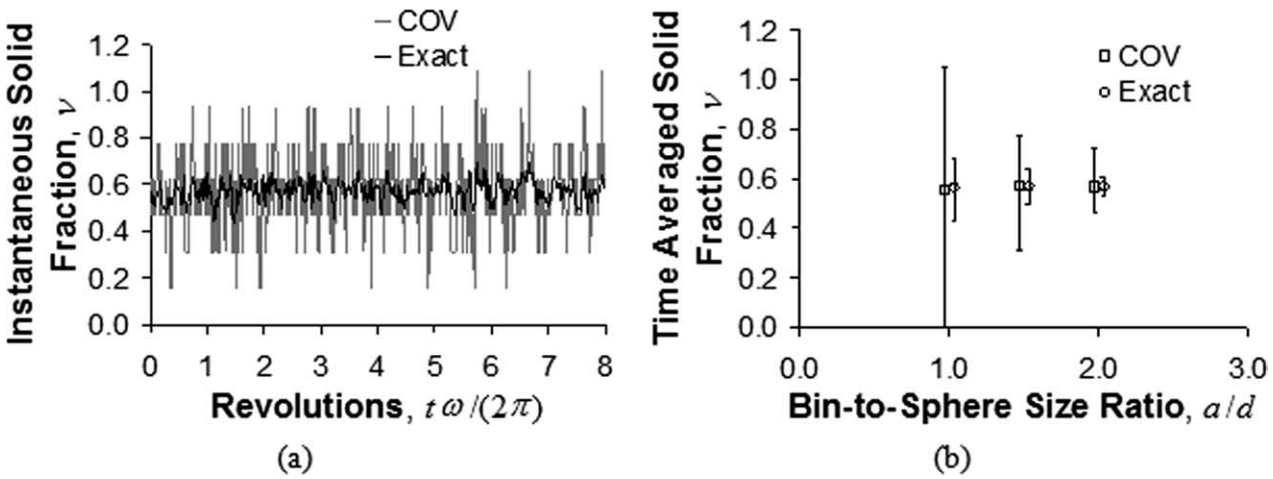

Figure 13. (a) Instantaneous solid fraction plotted as a function of dimensionless time for a bin of size *a/d* = 1.5 located slightly below the free surface using both the exact and COV methods.

(b) Time averaged solid fraction (over eight drum revolutions) plotted as a function of the bin-to-sphere size ratio. The scatter bars indicate the range containing 90% of the solid fraction measurements. The points are offset slightly for clarity; the values are actually located at $a/d = 1.0$, 1.5, and 2.0.

Literature Cited

1. Zhu HP, Yu AB. Averaging method of granular materials. *Phys Rev E*. 2002;66:021302.
2. Babic M. Average balance equations for granular materials. *Int J Eng Sci*. 1997;35:523–548.
3. Murdoch AI, Bedeaux D. Continuum equations of balance via weighted averages of microscopic quantities. *Proc Roy Soc: Math Phys Sci*. 1994;445:157–179.
4. Itasca Consulting Group, Inc. *PFC^{3D} (Particle Flow Code in 3 Dimensions) Theory and Background Version* 4.0, Minneapolis: ICG 2008.
5. Yang RY, Zou RP, Yu AB. Microdynamic analysis of particle flow in a horizontal rotating drum. *Powder Technol*. 2003;130:138–146.
6. Masson S, Martinez J. Effect of particle mechanical properties on silo flow and stresses from distinct element simulations. *Powder Technol*. 2000;109:164–178.
7. Mueller GE. Radial void fraction distributions in randomly packed fixed beds of uniformly sized spheres in cylindrical containers. *Powder Technol*. 1992;72:269–275.
8. Koval G, Roux JN, Corfdir A, Chevoir F. Annular shear of cohesionless granular materials: from the inertial to quasistatic regime. *Phys Rev E*. 2009;79:021306.
9. Schöllmann S. Simulation of a two-dimensional shear cell. *Phys Rev E*. 1999;59:59–70.
10. Theuerkauf J, Witt P, Schwesig D. Analysis of particle porosity distribution in fixed beds using the discrete element method. *Powder Technol*. 2006;165:92–99.
11. Mueller GE. Radial void fraction correlation for annular packed beds. *AIChE J*. 1999;45:2458–2460.
12. Govindarao VMH, Froment GF. Voidage profiles in packed beds of spheres. *Chem Eng Sci*. 1986;41:533–539.
13. Benenati RF, Brosilow CB. Void fraction distribution in beds of spheres. *AIChE J*. 1962;8:359–361.
14. Lätzel M, Luding S, Herrmann HJ. Macroscopic material properties from quasi-static, microscopic simulations of a two-dimensional shear-cell. *Granular Matter*. 2000;2:123–135.
15. Hrenya CM, Galvin JE, Wildman RD. Evidence of higher-order effects in thermally driven rapid granular flows. *J Fluid Mech*. 2008;598:429–450.
16. Karion A, Hunt ML. Energy dissipation in sheared granular flows. *J Heat Transfer*. 1999;121:984–991.
17. Karion A, Hunt ML. Wall stresses in granular Couette flows of mono-sized particles and binary mixtures. *Powder Technol*. 2000;109:145–163.
18. Lan Y, Rosato AD. Macroscopic behavior of vibrating beds of smooth inelastic spheres. *Phys Fluids*. 1995;7:1818–1832.
19. Loose W, Ciccotti G. Temperature and temperature control in nonequilibrium-molecular-dynamics simulations of the shear flow of dense liquids. *Phys Rev A*. 1992;45:3859–3861.
20. Campbell CS, Brennen CE. Computer simulations of granular shear flows. *J Fluid Mech*. 1985;151:167–188.
21. Lee J. Density waves in the flows of granular media. *Phys Rev E*. 1994;49:281–309.
22. Ristow GH, Herrmann HJ. Density patterns in two-dimensional hoppers. *Phys Rev E*. 1994;50:50–57.
23. Kumaran V. Dynamics of dense sheared granular flows. *J Fluid Mech*. 2009;632:109–144.
24. Khain E. Hydrodynamics of fluid-solid coexistence in dense shear granular flow. *Phys Rev E*. 2007;75:051310.
25. Wildman RD, Jenkins JT, Krouskop PE, Talbot J. A comparison of the predictions of a simple kinetic theory with experimental and numerical results for a vibrated granular bed consisting of nearly elastic particles of two sizes. *Phys Fluids*. 2006;18:073301.
26. Yang SC. Segregation of cohesive powders in a vibrated granular bed. *Chem Eng Sci*. 2006;61:6180–6188.
27. Zhong W, Xiong Y, Yuan Z, Zhang M. DEM simulation of gas-solid flow behaviors in spout-fluid bed. *Chem Eng Sci*. 2006;61:1571–1584.
28. Iordanoff I, Fillot N, Berthier Y. Numerical study of a thin layer of cohesive particles under plane shearing. *Powder Technol*. 2005;159:46–54.
29. GDR MiDi. On dense granular flows. *Eur Phys J E*. 2004;14:341–365.
30. Mitarai N, Nakanishi H. Hard sphere limit of soft-sphere model for granular materials: stiffness dependence of steady granular flow. *Phys Rev E*. 2003;67:021301.
31. Pöschel T, Salueña C, Schwager T. Scaling properties of granular materials. *Phys Rev E*. 2001;64:011308.
32. Buchholtz V, Pöschel T. Interaction of a granular stream with an obstacle. *Granular Matter*. 1998;1:33–41.
33. Khakhar DV, McCarthy JJ, Ottino JM. Radial segregation of granular mixtures in rotating cylinders. *Phys Fluids*. 1997;9:3600–3614.
34. Savage SB, Dai R. Studies of granular shear flows: wall slip velocities, "layering" and self-diffusion. *Mech Mater*. 1993;16:225–238.
35. Walton OR. Numerical simulation of inclined chute flows of monodisperse, inelastic, frictional spheres. *Mech Mater*. 1993;16:239–247.
36. Louge MY. Computer simulations of rapid granular flows of spheres interacting with a flat, frictional boundary. *Phys Fluids*. 1994;6:2253–2269.
37. Jenkins JT. Boundary conditions for rapid granular flow: flat frictional walls. *J Appl Mech*. 1992;59:120–127.
38. Krouskop PE, Talbot J. Mass and size effects in three-dimensional vibrofluidized granular mixtures. *Phys Rev E*. 2003;68:021304.
39. Jayasundrara CT, Yang RY, Yu AB, Curry D. Discrete particle simulation of particle flow in IsaMill-Effect of grinding medium properties. *Chem Eng J*. 2008;135:103–112.
40. Tsuji Y, Kawaguchi T, Tanaka T. Discrete particle simulation of two-dimensional fluidized bed. *Powder Technol*. 1993;77:79–87.
41. DEM-Solutions, Inc. *EDEM^{TM}, User Manual Version 2.1.2 (Revision 1)*, Edinburgh, Scotland: DEM-Solutions, Inc., 2009.
42. Hoomans BPB, Kuipers JAM, Briels WJ, van Swaaij WPM. Discrete particle simulation of bubble and slug formation in a two-dimensional gas-fluidized bed: a hard-sphere approach. *Chem Eng Sci*. 1996;51:99–118.
43. Hoomans BPB. *Granular Dynamics of Gas-Solid Two-Phase Flows*. PhD Thesis, The Netherlands: University of Twente, 2000.
44. Freireich B, Litster J, Wassgren C. Using the discrete element method to predict collision-scale behavior: a sensitivity analysis. *Chem Eng Sci*. 2009;64:3407–3416.
45. Hopkins MA, Louge MY. Inelastic microstructure in rapid granular flows of smooth disks. *Phys Fluids A*. 1991;3:47–57.
46. Tsuji Y, Tanaka T, Ishida T. Lagrangian numerical simulation of plug flow of cohesionless particles in a horizontal pipe. *Powder Technol*. 1992;71:239–250.

Appendix: Partial Sphere Volume Calculations

Derivations for the sphere/edge and sphere/corner overlap scenarios are presented in the following sections.

Sphere overlapping an edge

The shaded region in Figure A1 denotes the portion of a sphere overlapping a measurement bin edge. Points A and B lie on the surface of the sphere with x and y coordinates given by,

$$x_A = x_B = a \quad \text{and} \quad y_A = y_B = b \tag{37}$$

Note that on the surface of the sphere,

$$x^2 + y^2 + z^2 = r^2. \tag{38}$$

For the coordinates given in Eq. 37, the z coordinates for A and B are:

$$z_A = -\sqrt{r^2 - a^2 - b^2} \quad \text{and} \quad z_B = \sqrt{r^2 - a^2 - b^2}. \tag{39}$$

The volume of the section of sphere overlapping the edge (and denoted by hatched region) is:

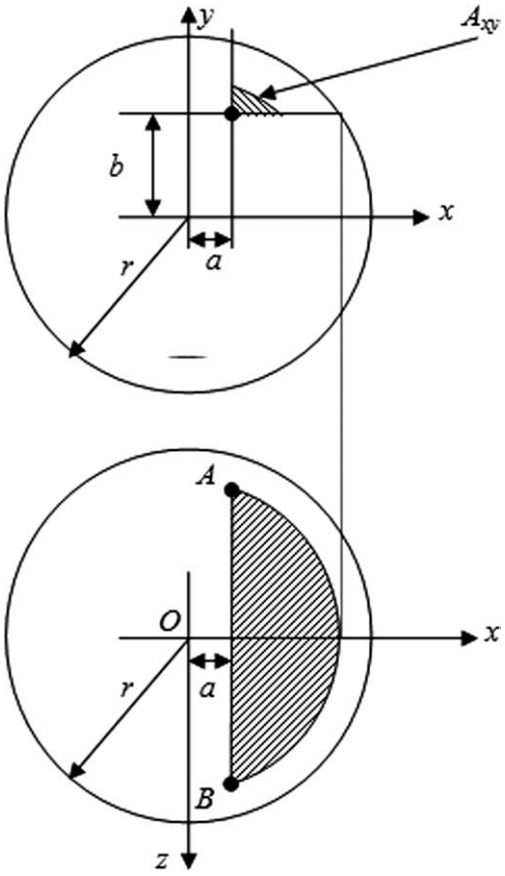

Figure A1. A sphere overlapping an edge boundary.

$$V_{\text{edge}} = 2\int_{z=0}^{z=\sqrt{r^2-a^2-b^2}} A_{xy}dz \tag{40}$$

where the boundary of the circle for the area A_{xy} is,

$$x^2 + y^2 = r^2 - z^2. \tag{41}$$

The limits of x and y for the area A_{xy} are:

$$x_{\min} = a \quad \text{and} \quad x_{\max} = \sqrt{r^2 - b^2 - z^2}, \tag{42}$$

$$y_{\min} = b \quad \text{and} \quad y_{\max} = \sqrt{r^2 - a^2 - z^2}, \tag{43}$$

For any z, the projected area A_{xy} is calculated as follows:

$$A_{xy} = \int_{y=y_{\min}}^{y=y_{\max}} [x(y) - x_{\min}]dy \tag{44}$$

where $x(y)$ is found by solving Eq. 41 for x. Explicitly,

$$A_{xy} = \int_{y=b}^{y=\sqrt{r^2-a^2-z^2}} \left(\sqrt{r^2 - y^2 - z^2} - a\right)dy \tag{45}$$

which simplifies to,

$$A_{xy} = ab - \frac{a}{2}\sqrt{r^2 - a^2 - z^2} - \frac{b}{2}\sqrt{r^2 - b^2 - z^2} + \frac{1}{2}(r^2 - z^2)\left[\tan^{-1}\left(\frac{-b}{\sqrt{r^2 - b^2 - z^2}}\right) - \tan^{-1}\left(\frac{-\sqrt{r^2 - a^2 - z^2}}{a}\right)\right] \tag{46}$$

Substituting this expression into Eq. 40, the volume of the overlapping section of sphere is:

$$V_{\text{edge}} = \frac{1}{3}\left[\begin{array}{l} 2ab\sqrt{r^2 - a^2 - b^2} + 2r^3\tan^{-1}\left(\frac{b\sqrt{r^2-a^2-b^2}}{ra}\right) + 2r^3\tan^{-1}\left(\frac{a\sqrt{r^2-a^2-b^2}}{rb}\right) \\ -(3br^2 - b^3)\tan^{-1}\left(\frac{\sqrt{r^2-a^2-b^2}}{a}\right) - (3ar^2 - a^3)\tan^{-1}\left(\frac{\sqrt{r^2-a^2-b^2}}{b}\right) \end{array}\right]. \tag{47}$$

In dimensionless form,

$$f_{\text{edge}} = \frac{V_{\text{edge}}}{\frac{4}{3}\pi r^3} = \frac{1}{4\pi}\left[2\hat{a}\hat{b}\hat{x} + 2\tan^{-1}\left(\frac{\hat{b}\hat{x}}{\hat{a}}\right) + 2\tan^{-1}\left(\frac{\hat{a}\hat{x}}{\hat{b}}\right) - \left(3\hat{b} - \hat{b}^3\right)\tan^{-1}\left(\frac{\hat{x}}{\hat{a}}\right) - \left(3\hat{a} - \hat{a}^3\right)\tan^{-1}\left(\frac{\hat{x}}{\hat{b}}\right)\right] \tag{48}$$

where $\hat{a} = \frac{a}{r}$, $\hat{b} = \frac{b}{r}$, and $\hat{x} = \sqrt{1 - \hat{a}^2 - \hat{b}^2}$.

Corner overlapping with sphere

The fractional sphere volume overlapping the corner of a measurement bin can be found using Eq. 40, but with a change to the limits of integration:

$$V_{\text{corner}} = \int_{z=c}^{z=\sqrt{r^2-a^2-b^2}} A_{xy}dz, \tag{49}$$

or written in a slightly different form,

$$V_{\text{corner}} = \tfrac{1}{2}V_{\text{edge}} - \int_{z=0}^{z=c} A_{xy}dz. \tag{50}$$

The second term in Eq. 50 simplifies to,

$$\int_{z=0}^{z=c} A_{xy}dz = \frac{1}{6}\begin{bmatrix} 6abc - 2ac\sqrt{r^2-a^2-c^2} - 2bc\sqrt{r^2-b^2-c^2} \\ -(3ar^2-a^3)\tan^{-1}\left(\frac{c}{\sqrt{r^2-a^2-c^2}}\right) + 2r^3\tan^{-1}\left(\frac{bc}{r\sqrt{r^2-b^2-c^2}}\right) \\ +(c^3-3cr^2)\tan^{-1}\left(\frac{b}{\sqrt{r^2-b^2-c^2}}\right) - (3br^2-b^3)\tan^{-1}\left(\frac{c}{\sqrt{r^2-b^2-c^2}}\right) \\ +2r^3\tan^{-1}\left(\frac{ac}{r\sqrt{r^2-a^2-c^2}}\right) + (3cr^2-c^3)\tan^{-1}\left(\frac{\sqrt{r^2-a^2-c^2}}{a}\right) \end{bmatrix} \tag{51}$$

Substituting into Eq. 50 and writing in dimensionless form,

$$f_{\text{corner}} = \frac{V_{\text{corner}}}{\frac{4}{3}\pi r^3}\begin{cases} \frac{1}{2}f_{\text{edge}} - \frac{1}{8\pi}\left\{ \begin{array}{l} 6\hat{a}\hat{b}\hat{c} - 2\hat{a}\hat{A}\hat{c} - 2\hat{b}\hat{B}\hat{c} - \left(3\hat{b}-\hat{b}^3\right)\tan^{-1}\left(\frac{\hat{c}}{\hat{B}}\right) - \left(3\hat{a}-\hat{a}^3\right)\tan^{-1}\left(\frac{\hat{c}}{\hat{A}}\right) \\ +(3\hat{c}-\hat{c}^3)\left[\tan^{-1}\left(\frac{\hat{A}}{\hat{a}}\right) - \tan^{-1}\left(\frac{\hat{b}}{\hat{B}}\right)\right] + 2\left[\tan^{-1}\left(\hat{c}\frac{\hat{a}}{\hat{A}}\right) + \tan^{-1}\left(\hat{c}\frac{\hat{b}}{\hat{B}}\right)\right] \end{array} \right\} & \text{for } \hat{a}^2+\hat{b}^2+\hat{c}^2 < 1 \\ 0 & \text{for } \hat{a}^2+\hat{b}^2+\hat{c}^2 \geq 1 \end{cases} \tag{52}$$

where $\hat{a} = a/r$, $\hat{b} = b/r$, $\hat{c} = c/r$, $\hat{A} = \sqrt{1-\hat{a}^2-\hat{c}^2}$, and $\hat{B} = \sqrt{1-\hat{b}^2-\hat{c}^2}$.

Manuscript received Oct. 9, 2009, and revision received Feb. 12, 2010.